Simulation of Beam Width and Position Measurement Using Optical Diffraction Radiation

David Yu
(Dated: September 9, 2008)

Optical diffraction radiation (ODR) is a promising technique for performing noninvasive beam diagnostics. The technique places a metal target near the beam line, which intercepts the virtual quanta associated with the relativistic motion of the beam. The virtual quanta are reradiated, and the resulting intensity distribution on the target is imaged. Features of the intensity distribution are correlated with beam size and position. Here I present the results of a simulation of measurements of beam width and position using ODR. The effects of variations in impact parameter and wavelength on the sensitivity of ODR imaging to changes in beam size and position are explored.

INTRODUCTION

Optical diffraction radiation (ODR) is a promising technique for performing beam diagnostics in a noninvasive manner. Techniques such as wire scanners are disadvantageous in that they interact directly with the beam, degrading beam quality as well as decreasing detector lifetime. Further, the ODR technique has potential to measure beam width and position simultaneously.

ODR is described through the Weizsacker-Williams virtual quanta method. The model exploits the similarity between the electromagnetic fields of a relativistic particle and the fields of photons, called virtual quanta. When a metal target is placed near the beam, the virtual quanta interact with the electrons in the target, which emit photons. To perform beam diagnostics, the resulting intensity distribution on the target is imaged and features of the distribution are correlated to beam parameters.

Here, we explore the application of ODR imaging to measurements of beam width and position. In particular, it is shown that the width of the perpendicularly polarized intensity distribution and the ratio of minimum to maximum in the parallel polarized component are strongly correlated with beam width. The beam position can be measured using the variation in intensity on the target. The simulations use the parameters listed in table 1, corresponding to the APS and the Tevatron.

	APS	TEV
γ	14000	1000
σ_x	100μm	400μm
σ_y	20μm	100μm
b	13σ_y	8σ_y
λ_c	120nm	20μm

FIG. 1: APS and Tevatron parameters

OPTICAL DIFFRACTION RADIATION

The application of the Weizsacker-Williams virtual quanta method is depicted in figure 2. The fields of a relativistic particle are equivalent to those of a photon traveling parallel to the beam (the longitudinal component of the fields, inversely proportional to γ, is neglected here). The virtual quanta interact with the metal target in the same manner as real photons, and consequently, real photons are reflected off the metal target, as shown in figure 3.

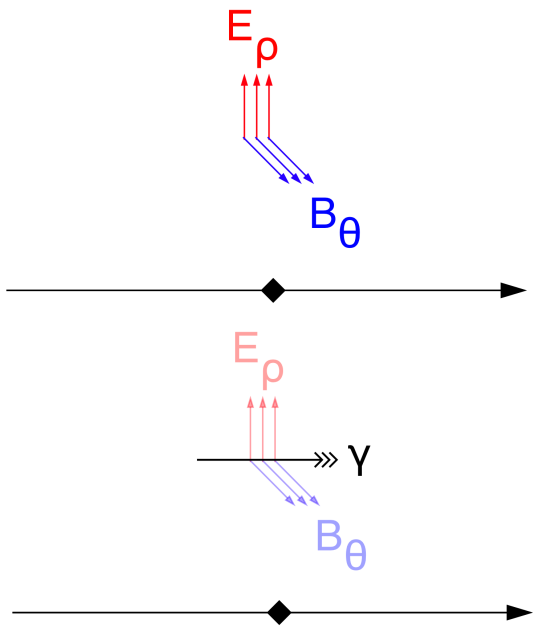

FIG. 2: Virtual quanta in the Wiesacker-Williams method

Derivation of Intensity Distribution

To calculate the intensity distribution on the target, we first calculate the Fourier transform of the

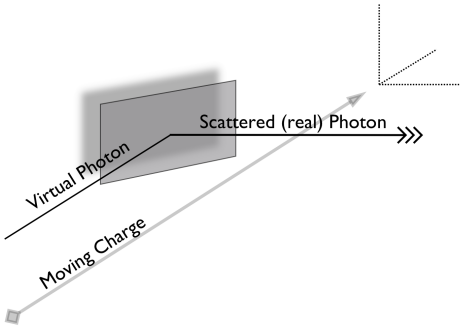

FIG. 3: ODR beam width monitoring schematic

relativistic particle's fields. The fields of a charge moving along the z-axis are:

$$\begin{aligned} E_\rho &= \frac{q\gamma\rho}{(\rho^2+(\gamma vt)^2)^{\frac{3}{2}}} \\ E_z &= -\frac{q\gamma vt}{(\rho^2+(\gamma vt)^2)^{\frac{3}{2}}} \end{aligned}$$

$\hat{E}_\rho(\omega)$ is calculated as follows:

$$\begin{aligned} \hat{E}_\rho(\omega) &= \int_{-\infty}^{\infty}\frac{dt}{2\pi}\frac{q\gamma\rho}{(\rho^2+(\gamma vt)^2)^{\frac{3}{2}}}e^{i\omega t} \\ &= \frac{2q\gamma\rho}{2\pi}\int_0^\infty \frac{cos(\omega t)dt}{(\rho^2+(\gamma vt)^2)^{\frac{3}{2}}} \end{aligned}$$

Let $s=\gamma vt$

$$\begin{aligned} &= \frac{q\gamma\rho}{\pi}\int_0^\infty \frac{\cos(\frac{\omega s}{\gamma v})ds}{\gamma v(\rho^2+s^2)^{3/2}} \\ &= \frac{q\rho}{\pi v}K_1\left(\frac{\omega\rho}{\gamma v}\right)\frac{\omega}{\gamma v\rho} \\ &= \frac{q\alpha}{\pi v}K_1(\alpha\rho) \end{aligned}$$

where $\alpha=\frac{\omega}{\gamma v}$ and K_1 is a modified Bessel function of the first kind. $\hat{E}_z(\omega)$ is calculated similarly:

$$\begin{aligned} \hat{E}_z(\omega) &= \int_0^\infty \frac{dt}{2\pi}\frac{-q\gamma vt}{(\rho^2+(\gamma vt)^2)^{3/2}}e^{i\omega t} \\ &= -\frac{iq\gamma v}{\pi}\int_0^\infty \frac{\sin(\omega t)tdt}{(\rho^2+(\gamma vt)^2)^{3/2}} \\ &= -\frac{iq\gamma v}{\pi}\int_0^\infty \left\{dt\sin(\omega t)\frac{-1}{\gamma^2v^2}\times \right. \\ &\quad \left.\frac{d}{dt}\left[\frac{1}{(\rho^2+(\gamma vt)^2)^{1/2}}\right]\right\} \\ &= \frac{iq}{\pi\gamma v}\int_0^\infty dt\sin(\omega t)\frac{d}{dt}\left[\frac{1}{\sqrt{\rho^2+(\gamma vt)^2}}\right] \\ &= -\frac{iq}{\pi\gamma v}\int_0^\infty \frac{\omega\cos(\omega t)dt}{(\rho^2+(\gamma vt)^2)^{1/2}} \end{aligned}$$

Let $s=\gamma vt$

$$\begin{aligned} &= -\frac{iq}{\pi\gamma v}\int_0^\infty \frac{\omega ds}{\gamma v}\frac{\cos\left(\frac{\omega s}{\gamma v}\right)}{(\rho^2+s^2)^{1/2}} \\ &= -\frac{iq\alpha}{\pi\gamma v}K_0(\alpha\rho) \end{aligned}$$

Note that the longitudinal field is inversely proportional to γ; for the Tevatron and APS energies, the longitudinal field is several orders of magnitude smaller than the transverse fields.

We now calculate the differential intensity distribution on the target. The Poynting vector (in Gaussian units) is given by

$$\mathbf{S} = \frac{c}{4\pi}\mathbf{E}\times\mathbf{B}^*$$

In the rest frame of the particle, $\mathbf{B'}=0$; since the fields transform as $B'_\perp=\gamma(B_\perp-|\beta\times\mathbf{E}|)$, this yields $B_x=-\beta E_y$ and $B_y=\beta E_x$, and

$$\mathbf{S} = \frac{c}{4\pi}\left[-\beta E_z E_x^*\hat{x}-\beta E_z E_y^*\hat{y}+\beta(|E_x|^2+|E_y|^2)\hat{z}\right]$$

Since we have neglected the longitudinal field components, we need only consider the $\hat{z}$ component of $\mathbf{S}$; regardless, the longitudinal field components lead to an inductive term in the intensity spectrum, which does not cause radiation. Here we consider a target oriented perpendicularly to the beam (in practice the target would be inclined with respect to the beam so that the ODR can be imaged away from the beam line. This complicates analysis of the diffraction that occurs between the target and the camera, but only causes a scale factor in the intensity distribution.) The total power incident on the target is

$$\begin{aligned} \Delta P &= \mathbf{S}\cdot\Delta\mathbf{A} = \mathbf{S}\cdot\hat{n}\Delta A \\ &= \frac{\beta c}{4\pi}\left[|E_x|^2+|E_y|^2\right]\Delta A \end{aligned}$$

With $\Delta P = \frac{d}{dt}\Delta W$, we define $I = \frac{\Delta W}{\Delta A}$, so that

$$\begin{aligned} \frac{dI}{dt} &= \frac{\beta c}{4\pi}[|E_x|^2 + |E_y|^2] \\ I &= \frac{\beta c}{4\pi}\int |E_x|^2 + |E_y|^2 dt \end{aligned}$$

Using Parseval's theorem,

$$\int |E_x|^2 dt = 2\pi \int |\hat{E}_x(\omega)|^2 d\omega$$

we obtain

$$\begin{aligned} \frac{dI}{d\omega} &= \frac{\beta c}{2}\left[|\hat{E}_x(\omega)|^2 + |\hat{E}_y(\omega)|^2\right] \\ &= \frac{\beta c}{2}|\hat{E}_\rho(\omega)|^2 \\ &= \frac{\beta c}{2}\left(\frac{q\alpha}{\pi v}\right)|K_1(\alpha\rho)|^2 \end{aligned}$$

To account for the finite size of the beam, this single-particle result is convoluted with the beam distribution function, yielding

$$\begin{aligned} \frac{dI}{d\omega} = \int\int \Bigg\{ dxdy \frac{\beta c}{2}\left(\frac{q\alpha}{\pi v}\right)^2 K_1^2(\alpha(\mathbf{r}_p - \mathbf{r}))\times \\ \frac{N}{2\pi\sigma_x\sigma_y}\exp\left[-\frac{(x-x_0)^2}{2\sigma_x^2} - \frac{(y-y_0)^2}{2\sigma_y^2}\right]\Bigg\} \end{aligned}$$

where (x_0, y_0) is the beam centroid, $\mathbf{r}_p$ is the point of observation, and $\mathbf{r}$ is the variable of integration.

To consider the perpendicular and parallel polarized components, we simply add the appropriate trigonometric factor, e.g.

$$\begin{aligned} \frac{dI_\perp}{d\omega} = \frac{N}{2\pi\sigma_x\sigma_y}\int\int \Bigg\{ dxdy \frac{(y-y_0)^2}{(x-x_0)^2 + (y-y_0)^2}\times \\ \frac{\beta c}{2}\left(\frac{q\alpha}{\pi v}\right)^2 K_1^2(\alpha(\mathbf{r}_p - \mathbf{r}))\times \\ \exp\left[-\frac{(x-x_0)^2}{2\sigma_x^2} - \frac{(y-y_0)^2}{2\sigma_y^2}\right]\Bigg\} \end{aligned}$$

The total and polarized differential intensity distributions are plotted in figure 4, using the APS parameters. The total intensity contours exhibit spherical symmetry, while the polarized intensity contours have a double-lobed pattern with a minimum perpendicular to the direction of polarization.

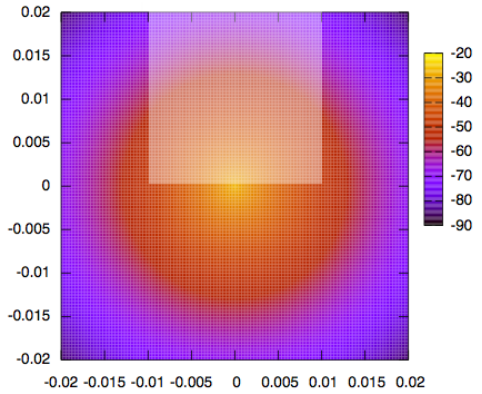

(a)Total intensity

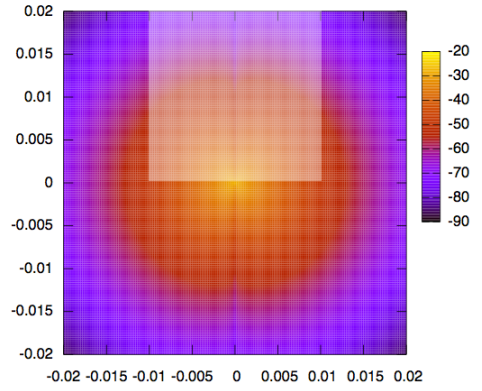

(b)Parallel polarized intensity

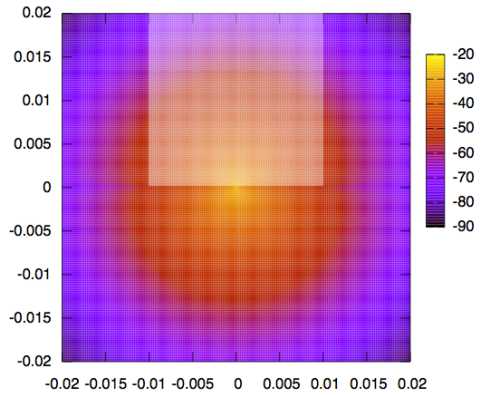

(c)Perpendicular polarized intensity

FIG. 4: Intensity contours, with rectangular target

BEAM WIDTH MEASUREMENT

Two features of the intensity distribution, the full width-half maximum (FWHM) of the perpendicular polarized (with respect to the target edge) distribution and the furrow in the parallel polarized distribution, show correlation with beam width. Figure 5 shows the intensity distribution along the edge of the target in figure 4. The parallel polarized distribution shows a distinctive peak-valley contour.

The dependence of the peak-valley shape on beam

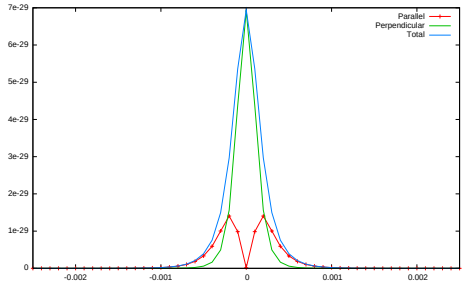

FIG. 5: Total and polarized intensity distribution along target edge

width is shown in figure 6. As the beam width σ_x increases, the valley becomes less pronounced. This correlation is quantified by taking the ratio of the central minimum to the maximum (MNMX), as shown in figure 7. The FWHM shows a similar positive correlation with beam width, shown in figure 8.

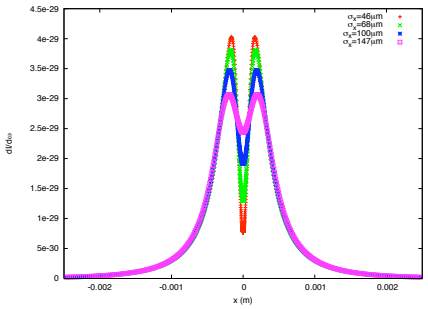

FIG. 6: Parallel polarized intensity along the target edge for different beam widths

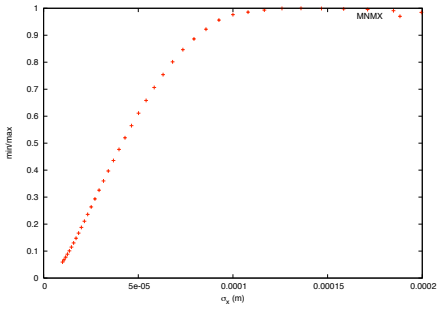

FIG. 7: MNMX vs σ_x for APS parameters

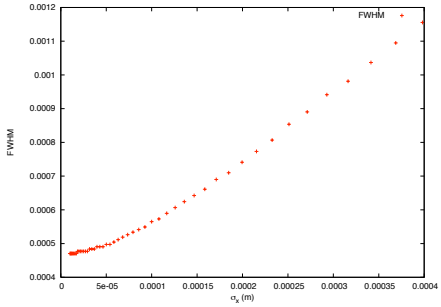

FIG. 8: FWHM vs σ_x for APS parameters

Sensitivity to Impact Parameter

In this section, the sensitivity of the MNMX and FWHM plots to the impact parameter of the beam is analyzed. In general, the target will not be closer than about $5\sigma_y$ for a lepton collider and $8\sigma_y$ for a hadron collider. The intensity of radiation decreases with impact parameter, as shown in figure 9; however, the shapes of the MNMX and FWHM curves change as well, and the impact parameter must be chosen so that there is both an observable amount of radiation and an appreciable variation in MNMX and FWHM over the expected range of beam width variation.

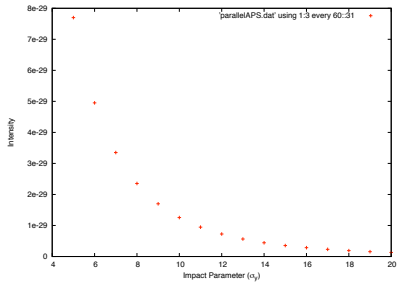

FIG. 9: Parallel Polarized Intensity vs. Impact Parameter, APS

The MNMX and FWHM curves are plotted for a range of impact parameters in figure 10. To maximize sensitivity to beam width variations, it is desired to have a large variation in MNMX or FWHM around the nominal beam width. In both the APS and the Tevatron examples, MNMX shows greater variation at smaller beam widths, while FWHM shows greater variation at beam widths larger than the nominal beam width. Figure 11 shows the derivative of the MNMX plots. Based on figure 11, we choose a nominal impact parameter of 11-14σ_y

for the Tevatron example and 7-9σ_y for the APS example.

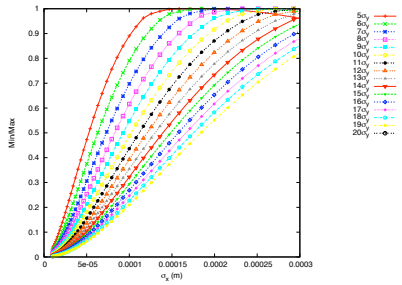

(a)MNMX, APS

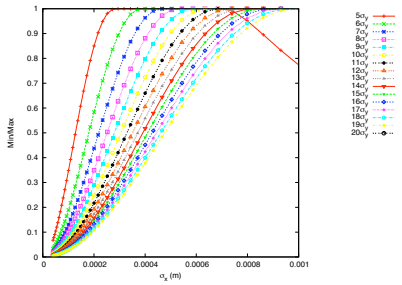

(b)MNMX, Tevatron

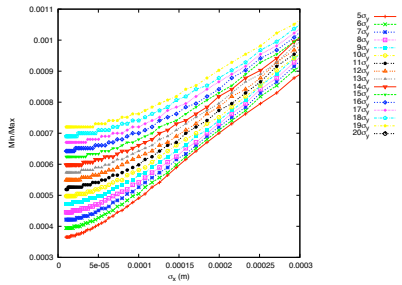

(c)FWHM, APS

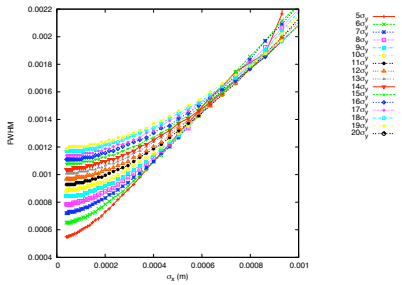

(d)FWHM, Tevatron

FIG. 10: MNMX and FWHM vs. beam width (σ_x) for several impact parameters.

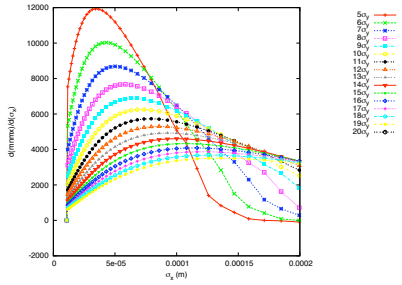

(a)Derivative of MNMX, APS

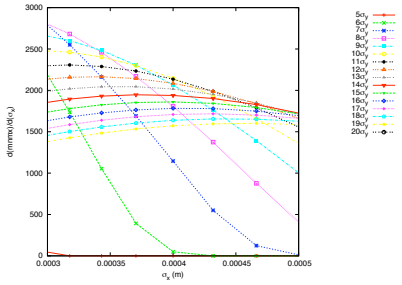

(b)Derivative of MNMX, Tevatron

FIG. 11: Derivative of MNMX with respect to beam width vs. beam width for several impact parameters

Derivative of MNMX with respect to the beam width as a function of the beam width for several impact parameters

Sensitivity to Wavelength

Here we consider the variation of intensity with wavelength, the variation in the FWHM and MNMX curves with wavelength, and the effect of the camera wavelength filter.

Intensity Variation

The Bessel function $K_1(x)$ has the asymptotic form $K_1(\alpha\rho) \approx \frac{1}{x}$ for $x \ll 1$. In the limit $\alpha\rho = \frac{\omega\rho}{\gamma v} \ll 1$, the intensity distribution becomes

$$\begin{aligned}\frac{dI}{d\omega} &= \frac{N}{2\pi\sigma_x\sigma_y}\int\int\left\{dxdy\frac{\beta c}{2}\left(\frac{q\alpha}{\pi v}\right)^2\left(\frac{1}{\alpha(\mathbf{r}_p-\mathbf{r})}\right)^2\times\right.\\ &\qquad\left.\exp\left[-\frac{(x-x_0)^2}{2\sigma_x^2}-\frac{(y-y_0)^2}{2\sigma_y^2}\right]\right\}\\ &= \frac{N\beta c}{4\pi\sigma_x\sigma_y}\left(\frac{q}{\pi v}\right)\int\int\left\{dxdy\frac{1}{(\mathbf{r}_p-\mathbf{r})^2}\times\right.\\ &\qquad\left.\exp\left[-\frac{(x-x_0)^2}{2\sigma_x^2}-\frac{(y-y_0)^2}{2\sigma_y^2}\right]\right\}\end{aligned}$$

Thus for large wavelengths, the intensity distribution is independent of wavelength. The scale of this approximation is given by

$$\begin{aligned}\frac{2\pi\rho c}{\gamma v\lambda_c} &\approx 1\\ \lambda_c &\approx \frac{\gamma}{2\pi b}\end{aligned}$$

where we have taken $v \approx c$ and $\rho \approx b$. This corresponds to $\lambda_c = 116$nm for the APS parameters and $\lambda_c = 20\mu$m for the Tevatron parameters. The intensity falls off rapidly below λ_c; this indicates the use of optical radiation for the APS example, and infrared radiation for the Tevatron example. Radiation below the critical wavelength must be used for the Tevatron, however, due to the restriction of camera technology to the near-infrared.

MNMX and FWHM Variation

Figure 12 shows the MNMX and FWHM curves for various wavelengths. As expected, above the critical wavelength there is little change. Below the critical wavelength, the general shape of the curves remains the same. For the APS parameters, optical radiation above the critical wavelength will be employed, so there is no effect on the shapes of the MNMX and FWHM curves. For the Tevatron

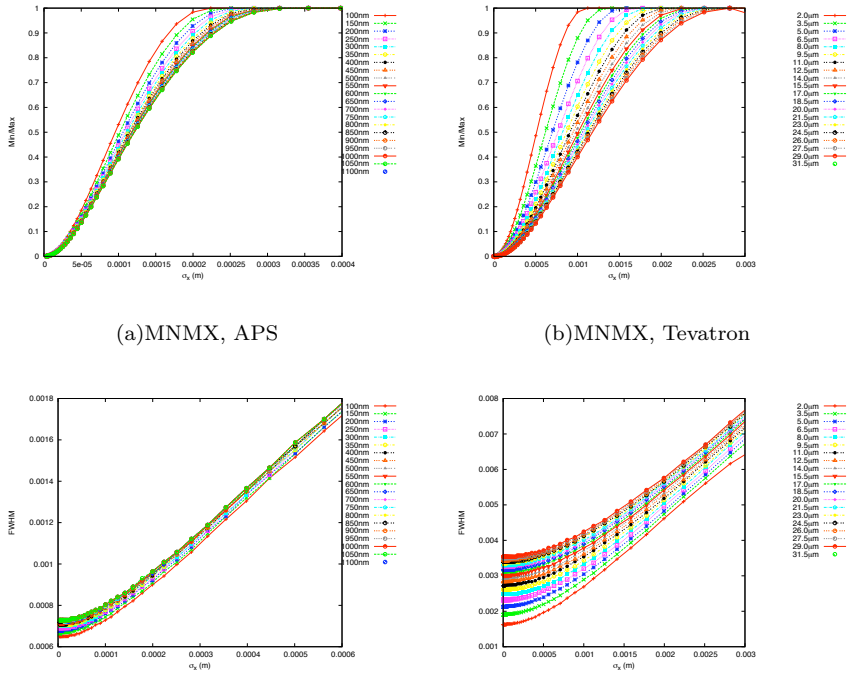

(a)MNMX, APS (b)MNMX, Tevatron

(c)FWHM, APS (d)FWHM, Tevatron

FIG. 12: MNMX and FWHM vs. beam width (σ_x) for several wavelengths

parameters, radiation well below the critical wavelength will be employed. In figure 12-b, the curves corresponding to near-infrared radiation show appreciable variation around the nominal beam width of 400μm. In both cases, the effect of wavelength on the shapes of the MNMX and FWHM curves is small.

Wavelength Range

Since a detector integrates over a range of wavelengths, accurate and simple determination of MNMX and FWHM values requires minimization of the variation in MNMX or FWHM with wavelength. Normalized values of MNMX and FWHM are plotted against wavelength for fixed beam size and impact parameter in figure 13. FWHM increases with wavelength, while MNMX decreases with wavelength. For the APS example, the variation of MNMX and FWHM with wavelength stabilizes towards the upper end of the optical spectrum. For the Tevatron example, the variation of MNMX and FWHM with wavelength stabilizes at much higher wavelength, near tens of microns; to accurately determine MNMX and FWHM values, a deconvolution algorithm would need to be applied.

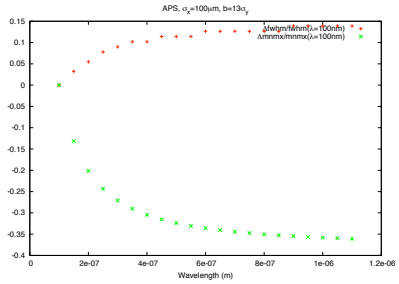

(a)APS

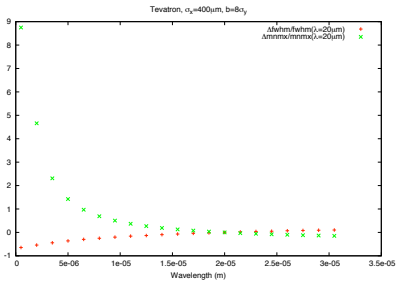

(b)Tevatron

FIG. 13: MNMX and FWHM vs Wavelength for fixed beam size and impact parameter

Summary

For the APS example, the use of wavelengths towards the upper optical range gives higher intensities and less variation in MNMX and FWHM over the camera wavelength range. Due to available infrared technology, the Tevatron example suffers from two drawbacks: the detector must operate below the critical wavelength, and the MNMX and FWHM values vary significantly over the range of detector wavelengths.

BEAM POSITION MONITORING

We hope to adapt the ODR technique to beam position monitoring as well as beam width measurement. Two possible methods of determining the beam position and the range of position variation are considered here: absolute intensity measurement and observation of minima and maxima positioning.

Absolute Intensity Measurement

Figure 14 shows the variation of intensity with impact parameter. The intensity ostensibly varies with impact parameter in a predictable manner; hence it could be possible to determine the impact parameter instantaneously by measuring the intensity at a fixed point of the target and comparing the value measured to a table.

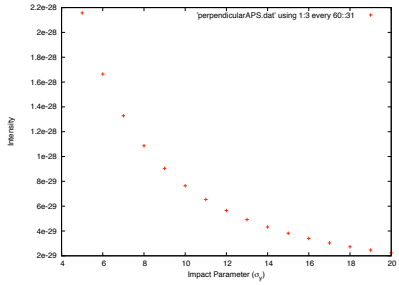

FIG. 14: Perpendicularly Polarized Intensity Vs. Impact Parameter, APS

Minima and Maxima Positioning

The intensity features used to determine beam width could also be used to determine beam position. In particular, the maximum of the perpendicularly polarized intensity and the minimum of the

parallel polarized intensity are aligned with the location of the beam. Figure 15 shows a polarized intensity distribution without target. The beam position, indicated by the black dot, is aligned with the furrow (corresponding with the intensity minima) in the vertical direction, and with the peak (corresponding to the intensity maxima) in the horizontal direction. An L-shaped target could be employed to determine the location of the beam in two dimensions.

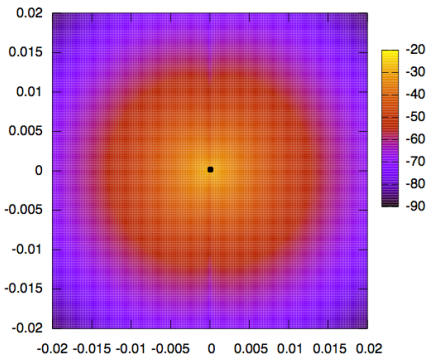

FIG. 15: Polarized intensity distribution with beam location indicated

CONCLUSION

This simulation has detailed two aspects of optimizing the ODR beam diagnostic technique. The impact parameter affects the magnitude of intensity and the shape of the MNMX and FWHM curves. Its value should be chosen to yield maximum variation in MNMX and FWHM around the nominal beam width, e.g. chosen to yield the maximum sensitivity to beam width variation. The wavelength range chosen affects the magnitude of intensity, the accuracy and simplicity of determining MNMX and FWHM values, and the shape of the MNMX and FWHM curves to a small extent. Ideally, we would like to have large intensity and little variation in MNMX and FWHM with wavelength. This is satisfied in the upper optical range for the APS parameters, but around 20μm for the Tevatron parameters. Since detector technology limits us to the near infrared, applying the ODR technique in the Tevatron example suffers from operating at submaximal intensities, and would require a deconvolution algorithm to determine MNMX and FWHM values.

It remains to account for the diffractive effects as the radiation propagates from the target, through a focusing lens, and to the camera. The limit of the far field approximation scales as γ^2, hence it may be necessary to consider the Fresnel regime, especially for lepton colliders.